https://doi.org/10.5194/egusphere-2025-4762
Preprint. Discussion started: 9 October 2025

Bottom topography effects on abyssal diapycnal mixing in the Eastern Mediterranean Sea

Florian Kokoszka[1,2], Stefania Sparnocchia[2], Davide Cavaliere[3], Vincenzo Artale[3], Mireno Borghini[4], Beatrice Giambenedetti[5], Federico Falcini[3*]

[1]Stazione Zoologica Anton Dohrn, Villa Comunale, Naples 80121, Italy
[2]Istituto di Scienze Marine, Consiglio Nazionale delle Ricerche, Trieste 34149, Italy
[3]Istituto di Scienze Marine, Consiglio Nazionale delle Ricerche, Roma 00133, Italy
[4]Istituto di Scienze Marine, Consiglio Nazionale delle Ricerche, Lerici 19032, Italy
[5]Istituto Nazionale di Geofisica e Vulcanologia, Roma 00143, Italy

*** Correspondence:**
Federico Falcini
federico.falcini@cnr.it

Keywords: Ionian Sea, diapycnal mixing, internal waves, shear and strain ratio, turbulent kinetic energy.

Abstract

The abyssal Ionian Sea is a deep region of interest for the entire ocean circulation of the Mediterranean Sea, since it plays an important role in the ventilation processes of the whole basin. Here we investigate spatial patterns of diapycnal mixing due to internal waves, over the bottom of the Ionian sub-basin. To identify regional features of the internal wave field in terms of vertical shear and strain, we analyze LADCP and CTD profiles, measured across the basin in 2007, covering various seafloor morphologies (shelf, shelf break, and abyssal plain). Our results show that increasing seafloor roughness reduces the variability of the shear-to-strain ratio, a pattern also influenced by correlations between slope and roughness. Roughness appears to constrain waves toward higher frequencies, with high shear-to-strain ratios associated with lower frequencies and flatter propagation angles, and low ratios linked to higher frequencies and steeper beams. Spectral analyses indicate that rougher regions enhance strain variance at small vertical scales while reducing shear variance at larger scales, leading to flatter shear spectra in the low-wavenumber band. Together, these findings suggest that roughness redistributes energy from large-scale toward small-scale, fundamentally altering the balance of internal wave energy across scales. These results expand our insights for 3D ocean circulation models, providing useful knowledge for ad hoc parameterization of mixing that should capture abyssal, internal wave–driven processes in the Mediterranean Sea.

https://doi.org/10.5194/egusphere-2025-4762
Preprint. Discussion started: 9 October 2025

1 Introduction

The abyssal circulation, when particularly constrained by seabed topography, can bring to the generation of internal waves (IWs) that enhance finescale shear (i.e., vertical variation of the horizontal velocity) and strain (i.e., vertical gradient of isopycnal displacements) over rough bathymetry (Polzin et al., 1997). The resulting small-scale mixing, due to breaking of IWs, may cause upwelling of abyssal waters along sloping boundaries (Osborne and Burch, 1980; Walin, 1982; Wunsch and Ferrari, 2004; Garrett and Kunze, 2007; Nikurashin and Ferrari, 2013; Cavaliere et al., 2021; La Forgia et al., 2021). At basin scale, this implies that water parcels become heavier within the stratified ocean interior, while they result to become lighter along the oceanic boundaries; consequently, IW processes are likely responsible for transporting energy upward (Munk, 1966; Ferrari, 2014; Ferrari et al., 2016).

Despite its thorough implications in the ocean circulation, the relationship between the intensity of overturning circulation and deep, IW-induced mixing rates is not yet fully understood (Garrett and Laurent, 2002; Ferrari, 2014). Paucity of deep ocean measurements hampers our knowledge on abyssal mixing processes and, consequently, ocean heat content variability (Munk and Wunsch, 1998; Ferrari and Wunsch, 2009; Nikurashin and Ferrari, 2011; Waterhouse et al., 2014; de Lavergne et al., 2016; MacKinnon et al., 2017; Ferron et al., 2017; Artale et al., 2018). Few deep-ocean observations demonstrated that dissipation rates of turbulent kinetic energy, and the related changes of potential energy of the water column through diapycnal mixing, increase as the turbulent probes approached the ocean bottom above rough topography (Polzin et al., 1997; Ledwell et al., 2000; St. Laurent et al., 2012; Ferrari et al., 2016; Mashayek et al., 2017). The analysis of IW-field characteristics from microstructure and fine-structure observations suggests that bottom-generated IWs play a major role in determining the spatial distribution of turbulent dissipation (Sheen et al., 2013; Kunze et al., 2006; Ferron et al., 2014; Ferron et al., 2016). Recent observations indicate that IW field characteristics, shaped by local topography and forcing, show significant variability not only in amplitude but also in frequency composition, affecting the structure and energy distribution of the wave packets and the resulting turbulent mixing (Chinn et al., 2016). These considerations inspired us to investigate the potential role of IWs in mixing processes within the eastern part of the Mediterranean basin, where synchronous Lowered Acoustic Doppler Current Profiler (LADCP) and Conductivity, Temperature, Depth (CTD) data were available.

The Mediterranean Sea, due to its specific thermohaline, geographical, and morpho-bathymetric characteristics, as well as its intense convective and mixing processes, is one of the most interesting marginal seas of the global ocean (Schroeder et al., 2016; Artale et al., 2018). It is often considered as a “miniature ocean” due to its own thermohaline cell, where cold and/or salty waters sink during winter at specific regions and, subsequently, spread to intermediate and deep, near-bottom layers (Wüst, 1961; Bergamasco and Malanotte-Rizzoli, 2010; Millot and Taupier-Letage, 2005; Somot et al., 2006; Tsimplis et al., 2006). Moreover, among the Mediterranean-type climates, i.e., those defined by temperate, wet winters and hot/warm, dry summers over the western edges of five continents, the Mediterranean is the only one in which the atmospheric variability produces an intense deep-water formation (Seager et al., 2019).

Several analyses of the Mediterranean overturning circulation showed that this marginal basin is well ventilated, in comparison to the world ocean (Wüst, 1961; Malanotte-Rizzoli and Hecht, 1988;

https://doi.org/10.5194/egusphere-2025-4762
Preprint. Discussion started: 9 October 2025

Pinardi and Masetti, 2000; Theocharis et al., 2002; Artale et al., 2006; Malanotte-Rizzoli et al., 2014; Schneider et al., 2014). Negative hydrological balance and cold-dry winds, blowing during the winter season, make the Mediterranean Sea an extraordinary place of intense ocean water mass transformation (Pinardi and Masetti, 2000), and thus, an ocean laboratory to study the main processes involved in the global ocean circulation.

Surface water from the Atlantic Ocean enters the Mediterranean basin through the Strait of Gibraltar (Figure 1a), forming a shallow overturning circulation at the upper layer. Flowing eastward, along the African coasts, this Atlantic water increases its salinity and density, then sinking in the Levantine basin in the eastern Mediterranean and forming the Levantine Intermediate Water (LIW). The LIW flows back into the opposite direction, mixing with the surrounding water mass found along its travel back and leaving the Mediterranean Sea through the Strait of Gibraltar, which works as a salt-valve (Artale et al., 2006). Deep water exchanges between the western and the eastern Mediterranean basins occur within the shallow Sicily Channel (Figure 1a), which makes the deep-water circulation of the two sub-basins rather independent from each other (Sparnocchia et al., 1999; Napolitano et al., 2003; Béranger et al., 2004; Schroeder et al., 2006). In the eastern basin, the Eastern Mediterranean Deep Water (EMDW) is formed, alternately, in separate regions of the Eastern Mediterranean Sea (Figure 1a), i.e., the southern Adriatic Sea and the Aegean Sea (Gačić et al., 2010). This cold and high salinity winter water, after deep convection, flows into the Ionian Sea (Wüst, 1961; Roether and Schlitzer, 1991; Schlitzer et al., 1991; Roether et al., 1996; Bensi et al., 2013a; Bensi et al., 2013b; Bellacicco et al., 2016), i.e., the deepest sub-basin of the Mediterranean Sea, which has a maximum depth close to the mean depth of the global ocean (Figure 1a). Such a thermohaline circulation is, therefore, characterized by a superposition of intermediate and deep, zonal and meridional overturning cells (Bergamasco and Malanotte-Rizzoli, 2010).

In the Ionian Sea boundary currents show intense downwelling due to their interaction with the topographic constraints while the deepest part of the basin is characterized by extremely weak stratification (Waldman et al., 2018), which induces a deepening and barotropization of the flow (Holte and Straneo, 2017; Send and Testor, 2017). These deep waters are characterized by IW-turbulence and mixing (van Haren and Gostiaux, 2011). Moreover, the Ionian Sea shows a semi-diurnal lunar tidal (M2) and a dominant motion that is around the inertial frequency, mainly as freely propagating IWs (Gerkema and Zimmerman, 2008). For this reason, the Ionian Sea constitutes a unique example for studying the fundamental dynamics and processes of the abyssal layers in the Mediterranean basin, also in the light of turbulent mixing due to IW breaking (Rubino et al., 2012; Artale et al., 2018; Giambenedetti et al., 2024).

An intense observational activity was conducted in the Ionian Sea in the framework of the Cubic Kilometre Neutrino Telescope (KM3NeT) project, from April 2006 to May 2009 (Kats et al., 2006). During the KM3Net cruise (July 2007), hydrographic measurements were spread over a large area, including a section that almost synoptically spanned the central Ionian Sea, from Sicily to Greece. On the western side and up to the central abyssal plane, a marked stratification was found in the deep layers, with a warmer and saltier water on the bottom, below a fresher and slightly colder layer (located approximately at about 2750 m), probably due to deep water formation processes at different times (Sparnocchia et al., 2011). Deep current meter measurements collected in the westernmost part in the period 2007–2008 showed a quite energetic and impulsive abyssal circulation pattern, with maximum velocities up to 15 cm/s, alternating with periods of quiet, strongly affected by the bathymetric

https://doi.org/10.5194/egusphere-2025-4762
Preprint. Discussion started: 9 October 2025

constraints. Furthermore, cyclonic and anti-cyclonic mesoscale structures, with a period of 5-to-11 days, superimposed on the background flow, were identified (Rubino et al., 2012; Meccia et al., 2015).

Artale et al. (2018), by analyzing water column characteristics of the Ionian Sea, observed during the last three decades, focused on the hydrological processes occurring at the bottom layer. They found that the ocean circulation in this abyssal plain is strongly affected by an interplay between advection and diffusion. The progressive warming and salinification of this sub-basin produced warmer near-bottom waters, causing an anomalous heat storage of ~1.6 W/m^2, i.e., a value three times larger than the equivalent climate trend occurring in the same period at global scale (Bindoff et al., 2007). The analysis of Artale et al. (2018) investigated the triggering of a diapycnal mixing due to rough bathymetry. In particular, to explore topographic-induced mixing, these authors estimated dissipation rates from the "CTD strain-based" parameterization (Kunze et al., 2006), showing the role of the sea bottom in enhancing isopycnal vertical strain.

From the synergic use of LADCP and CTD data, collected in the Ionian Sea during the KM3Net cruise in 2007, here we expand the analysis of Artale et al. (2018) and we seek to provide new insights on the relation between IW mixing and bottom topographic constraints. In particular, we explore different seafloor characteristics, in terms of bathymetric gradient and bottom roughness. LADCP profiles, synchronous with CTD casts, allowed estimation of regional values of shear-to-strain ratio (R_ω) within the parameterization of kinetic energy dissipation rate ε_{iw} and, in turn, diapycnal diffusivity K_{iw} (Garrett and Munk, 1975; Munk, 1981; Kunze et al., 2006). In the frame of the Garrett-Munk parametrization (Polzin & Lvov, 2011; See Data and methods), we explore the relation between R_ω and topographic features of the Ionian Sea. This approach employs CTD profiles to determine the isopycnal vertical strain ($< \xi_z^2 >_{in\ situ}$), and LADCP profiles for the vertical shear of horizontal velocities ($< V_z^2 >_{in\ situ}$), assuming that the variance is due to the presence of IWs (See Data and methods). These variances are used to estimate the local energy's level of the IW field, to modulate a canonical value of the dissipation rate of turbulent kinetic energy ε_0 (Garrett and Munk, 1975).

2 Data and methods

2.1 Hydrological casts

Our analysis is based on CTD and LADCP profiles (Borghini et al., 2025) acquired in July 2007 during a research cruise aboard the R/V Urania, conducted within the framework of the KM3NeT project (https://www.km3net.org/). Hydrological stations were distributed over a wide area of the northwestern Ionian Sea (Figure 1a), including strategic sites for the KM3NeT (Neutrino Telescope) infrastructure that have been identified by the particle physics community (Katz, 2006).

CTD data were acquired from the sea surface to the bottom by using a SBE911-plus calibrated before the cruise at the NATO center in La Spezia and were processed by the SBE Sea Soft program, following the standard procedure suggested by the manufacturer. LADCP profiles were collected in a subset of stations using a dual-head system installed on the rosette made of two RDI BB/WH 300 kHz instruments looking upward and downward respectively. The instruments have been preset to acquire 20 bins with size 10.00 m and the LADCP data were processed using the LDEO LADCP software Version IX.13 (https://github.com/athurnherr/LDEO_IX/releases/tag/IX_13), using CTD and respective GPS fixes as auxiliary data.

https://doi.org/10.5194/egusphere-2025-4762
Preprint. Discussion started: 9 October 2025

2.2 Finescale parameterization

The small spatial scales (order of centimeters) and intermittent temporal nature (from minutes to hours) involved in internal-wave-driven turbulent mixing, imply that direct measurements are difficult to achieve. Indeed, measurements resolving small-scale turbulence rely on ship-based microstructure profilers, not yet in wide use and, in any case, not on board during the 2007 KM3NeT research cruise. To fill this gap, finescale parameterizations are being used to estimate the turbulent kinetic energy dissipation rate and diapycnal diffusivity from more common instruments, such as CTDs, ADCPs, and Argo profiles (Whalen et al., 2020; Polzin et al., 2014). Finescale parameterizations aim to infer the centimeter-scale turbulent energy dissipation rate, operating on the intermediate [O(10-100) m] vertical wavelengths that are assumed to mediate energy transfer between large and small scales in the ocean (Polzin et al., 2014). Finescale parameterizations are formulated by reference to the Garrett-Munk 75 model (hereafter, GM) (Garrett & Munk, 1975; Cairns & Williams, 1976; Polzin & Lvov, 2011), which provides an empirical expression for the internal wave energy density in the spectral domain. Strain- and shear-based parameterizations allow to estimate the in-situ internal wave energy level, which serves to establish a deviation from the GM model, and to adjust its canonical value for the turbulent dissipation rate ε_0 to a more realistic estimate. In particular, the turbulent dissipation rate can be expressed through a recent finescale parameterization proposed by Kunze et al. (2006) as:

$$\epsilon_{\mathrm{iw}} = \epsilon_0 \frac{N^2}{N_0^2} \left(\frac{E}{E_{GM}}\right)^2 F(R_\omega) L(f,N) \qquad (1)$$

where E is the in situ internal wavefield variance and N the in-situ Brünt-Väisälä frequency, while E_{GM}, $\varepsilon_0 = 7 \times 10^{-10} W/kg$ and $N_0 = 5.2 \times 10^{-3}\, rad/s$ are the GM internal wavefield variance, dissipation rate and Brünt-Väisälä frequency, respectively (Garrett and Munk, 1975; Munk, 1981). Depending on whether the parameterization is based on shear or strain, $(E_{in-situ}/E_{GM})^2$ in Eq. (1) can be estimated from the shear variance as $< V_z^2 >_{in-situ}^2 / < V_z^2 >_{GM}^2$, or from the strain variance as $< \xi_z^2 >_{in-situ}^2 / < \xi_z^2 >_{GM}^2$.

The factor $L(f,N)$ in (1) represents the latitude effect, calculated as $L(f,N) = f\, cosh^{-1}(N/f) \,/\, f_0\, cosh^{-1}(N_0/f_0)$ with f the Coriolis parameter and f_0 the Coriolis's frequency at 30°. The term R_ω represents the internal wavefield's aspect ratio and the bulk frequency content, and it is defined as the ratio of the buoyancy normalized shear variance to the strain variance:

$$R_\omega = (< V_z^2 > / N^2) / < \xi_z^2 >), \qquad (2)$$

https://doi.org/10.5194/egusphere-2025-4762
Preprint. Discussion started: 9 October 2025

whose effect on dissipation rates ϵ_{iw} is modeled by the term $F(R_\omega)$:

$$F(R_\omega) = h_1(R_\omega) = 3/4(1 + 1/R_\omega)\sqrt{2/(R_\omega - 1)} \quad \text{(for shear-based parameterization)} \quad (3a)$$

$$F(R_\omega) = h_2(R_\omega) = R_\omega(R_\omega + 1)/\left(6\sqrt{2R_\omega - 1}\right) \quad \text{(for strain-based parameterization)} \quad (3b)$$

In Equations (3a,b), for $R_\omega = 3$ (i.e., the GM value), the correction functions are equal to 1 and do not affect ε_{iw}. When $R_\omega > 3$, shear variance dominates, low-frequency internal waves contribute more strongly, and h_1 decreases (underestimates ε_{iw}), while h_2 increases (overestimates ε_{iw}). When $R_\omega < 3$, strain variance dominates, high frequency internal waves contribute more to the ratio: h_1 increases (overestimates ε_{iw}), h_2 decreases (underestimates ε_{iw}). This makes the shear-based parameterizations more reliable when $R_\omega > 3$, and conversely the strain-based parameterizations are more reliable when $R_\omega < 3$ (Chinn et al. 2016).

The determination of R_ω requires, ideally, shear and strain variance measurements through LADCP and CTD observations, respectively. The strain ξ_z is defined as the vertical derivative of the isopycnal displacement and is generally calculated as $\xi_z = (N^2 - N^2{}_{fit})/\overline{N^2}$, where N^2 is the Brünt-Väisälä frequency, $\overline{N^2}$ a mean value over the vertical segment of water column, and N^2_{fit} a polynomial quadratic fit: N^2 - N^2_{fit} represents the IW's density perturbation, normalized by $\overline{N^2}$ to obtain the vertical derivative of the isopycnal displacements.

Instead of determining ξ_z, we follow the approach of Ferron et al. (2014) and we determine ξ from the density fluctuations as $\xi = (g/\rho_0)(\rho_{HP}/\overline{N^2})$, with g/ρ_0 the standard gravity on the reference density, and ρ_{HP} density filtered by a high-pass Butterworth filter with a cutoff wavelength of 160m to remove the density fluctuations associated with the background stratification, whose signal would contaminate the integration of the strain spectra (Kunze et., al 2006). This advantageously avoids fitting a polynomial to N^2 (e.g., quadratic fit in Kunze et al., 2006), that could be inconsistent with the shape of the density profile in case of strong vertical gradients. Strain variance is then calculated as the integral of the isopycnal displacement spectra between k_{min} and k_{max}:

$$< \xi_z^2 >= \int_{k_{min}}^{k_{max}} k^2 S(\xi) dk. \quad (4)$$

Similarly, the shear $< V_z^2 >$ is obtained from the velocity spectra as

$$< V_z^2 >= \int_{k_{min}}^{k_{max}} k^2 S(u, v) dk. \quad (5)$$

https://doi.org/10.5194/egusphere-2025-4762
Preprint. Discussion started: 9 October 2025

231

232 To integrate the spectra, k_{min} and k_{max} must be carefully determined, as shear and strain rely on
233 different instrument limitations and can be sensitive to distinct phenomenological contributions.
234 In general k_{min} is fixed by the choice of the data segment length $k_{min} = 2\pi/L\ rad\ m^{-1}$, where L is
235 generally of 200-to-500 m, i.e., a compromise between the larger vertical wavelengths to be considered
236 (the spectral resolution to be employed) and the desired vertical resolution. For strain, in particular,
237 the integration is performed from $k_{min} = 2\pi/O(150m)$ (Kunze, 2006, Pollman, 2017; 2020), to
238 exclude contributions from larger-scale background stratification, and continues up to $k_{max} =$
239 $2\pi/10m$ (the GM upper limit).

240 For shear, a velocity noise is expected to dominate at high wavenumber, especially in weakly
241 stratified layers lacking turbulent microstructures or suspended material ("water-column reflectors")
242 (Kunze et al., 2006), which tend to reflect the acoustic signal emitted by Doppler profilers like the
243 LADCP. Their absence reduces the quality of the acoustic return, leading to higher measurement
244 uncertainty and potentially spurious velocity variance, especially at small vertical scales. Thus,
245 wavenumbers larger than $k_{max} = 2\pi/O(100 - 50m)$ represent the upper limit range of usable
246 vertical wavenumbers for integration.

247 An additional saturation criterion is applied to limit the integration of spectra (Gargett, 1990, Kunze
248 et al., 2006). Specifically, the integration is stopped when reaching the saturation value of $0.66\ N^2$ for
249 the shear variance and $0.22\ N^2$ for strain. This threshold represents the onset of internal wave breaking
250 or turbulence, where the linear internal wave regime breaks down. The corresponding vertical
251 wavenumber k_c at which this value is reached is retained as the upper limit for the integration. This
252 approach constrains the finescale parameterization to physically realistic shear and strain levels,
253 avoiding overestimation of internal wave energy due to instrument noise or unresolved scales,
254 particularly in regions of enhanced energy.

255 In our case, strain and shear are derived from CTD and LADCP measurements from the bottommost
256 640 m of each vertical profile. Signals are then linearly detrended and Fourier transformed with a
257 Hamming tapering window. Strain and shear variance estimates are obtained by integrating the 640 m
258 segments, overlapping every 10 m from the bottom to the surface, to account for non-homogeneity in
259 the statistical distribution of the water column properties and to have a more robust representation of
260 the fine-scale variability. Conveniently, final variances are obtained by averaging collections of
261 estimates over finite-sized segments (here 80 m).

262 The shear integration upper limit has been identified from the velocity error. The LADCP processing
263 (velocity-inversion method (Polzin, 2002), LDEO), provides a single-bin error profile for each station.
264 The average $\overline{V_{ERR}} = 0.075\ m.s^{-1}$ is used to estimate a velocity error by segment as $V_{NOISE} =$
265 $\overline{V_{ERR}}/\sqrt{640m/10m}$. Its associated variance ${V_{NOISE}}^2$ is then distributed on the spectral domain to
266 produce a white noise velocity spectrum that, once sheared, allows to obtain a shear noise spectrum
267 that will identify the noise-free upper limit in the spectral domain.

268 The resulting spectra are then averaged by stratification bins, as shown in Figure 1b, where we
269 highlighted their overall shape and the noise-free bandwidths we retain for integration, from 640 to
270 107 m. This choice is conservative, as our lowest stratification levels are close to the $N_{ERR} = 5 \cdot 10^{-4}$
271 s^{-1} (discussed in Kunze, 2006), and consistent with the integration set up of Ferron (2014) that stopped
272 the integration at 107 m in the most limitative case. Additionally, this treatment combined both data

https://doi.org/10.5194/egusphere-2025-4762
Preprint. Discussion started: 9 October 2025

from downward and upward profiles, in relatively small bin size (10 m), limiting then the expected variance loss at short scales due to the various steps of data processing (Polzin, 2002; Thurnherr, 2012). For strain, integration is led from 128 to 10 m (the GM upper limit).

Since shear and strain are integrated on their respective bandwidths, instead of using Eq. (2) directly, the shear-to-strain ratio is calculated as:

$$R_\omega = {R_\omega}^{GM}(< V_z^2 >/< V_z^2 >_{GM})/(< \xi_z^2 >/< \xi_z^2 >_{GM}), \quad (6)$$

where ${R_\omega}^{GM} = 3$, both shear and strain factors are divided by their associated value in the GM model, evaluated on the same spectral bandwidth, respectively. Finally, from Equations (1), (3), and (6), the kinetic turbulent diffusion rate $K_{iw} = \Gamma\varepsilon_{iw}/N^2$ is calculated with the Osborn-Cox relation (Osborn and Cox, 1972), using a mixing efficiency value of $\Gamma = 0.2$.

All functions used for obtaining Equation (6) are in Kokoszka, F. (2025).

2.3 Internal wave beams and impact of bathymetry on R_ω

Traditional finescale parameterizations of turbulent kinetic energy dissipation rely on the assumption that the internal wave field follows a GM-like structure. In this framework, a fixed value of the shear-to-strain ratio, typically $R_\omega \approx 3$, is used to represent the relative contributions of vertical shear and isopycnal strain to the finescale energy budget. This fixed value implicitly assumes a broadband, statistically stationary internal wave field, with no significant spatial variability in spectral composition. However, these models sometimes fail to capture the true dynamics near mixing hotspots where the internal wave spectra can be significantly distorted, showing bias toward higher or lower frequencies.

Accumulating evidence from both observations and modeling (Ijichi and Hibiya, 2015, 2017; Takahashi, et al. 2021; Dematteis et al., 2024) indicates that this assumption is often violated, especially in regions influenced by complex bathymetry, variable stratification, or energetic boundary currents. In these settings, the internal wave spectrum is distorted, leading to departures from the canonical balance between shear and strain. As a result, R_ω can vary significantly in space and time, reflecting changes in the dominant frequency content of the wave field.

Ijichi and Hibiya (2017) used 3D eikonal equations to simulate how internal waves transfer energy across distorted spectra, including variations in the wave energy level, the local buoyancy frequency, and the inertial frequency. Their results confirm that energy transfer rates are consistent with the Henyey et al. (1986) model, which predicts dissipation from internal wave-wave interactions and highlights the importance of the spectral shear-to-strain ratio R_ω. The study questions the accuracy of existing finescale parameterization models, particularly in environments with distorted spectra near boundaries or topographic features. To address these limitations, Ijichi and Hibiya (2015, 2017) propose a revised parameterization that explicitly considers both broadband and narrowband spectra.

https://doi.org/10.5194/egusphere-2025-4762
Preprint. Discussion started: 9 October 2025

This leads to more accurate dissipation estimates by incorporating a dynamically varying R_ω instead of assuming a constant value based on idealized spectral shapes. Their approach was further developed by Takahashi et al. (2021), who showed how vertical wavenumber spectra distortions (such as spectral humps) can bias traditional estimates, emphasizing the need to resolve the spatial variability of R_ω.

From a physical point of view, R_ω represents the ratio between the buoyancy-normalized vertical shear variance and the isopycnal strain variance. The spectral structure of the internal wave field determines whether energy is primarily stored in the shear (associated with horizontal motion) or in the strain (associated with vertical isopycnal displacement). The theoretical foundation for this lies in the internal wave dispersion relation:

$$\omega^2 = \frac{N^2 k_h^2 + f^2 {k_z}^2}{k_h^2 + {k_z}^2}, \tag{7}$$

where ω is the wave frequency, $\boldsymbol{k}_h = (k_x, k_y)$ and k_z the horizontal and vertical wavenumbers, respectively.

Equation (7) shows the intrinsic relation between horizontal (vertical) wavenumber and the shear-to strain ration. When $\omega \approx f$, it follows that $k_z \gg k_h$ and that the wavefield is dominated by horizontal motion, yielding high shear $\partial u / \partial z$, i.e., the wavefield varies rapidly with depth and more slowly in the horizontal direction. This configuration results in particle motions that are predominantly horizontal but vary significantly over short vertical distances. Consequently, the vertical gradient of horizontal velocity (i.e., the vertical shear) is amplified. Even when vertical displacements of isopycnals are small, the horizontal velocity field can exhibit strong vertical variation due to the short vertical wavelength (large k_z). This sharp vertical structure leads to high shear variance.

In realistic internal wave spectra, low-frequency components (near the Coriolis frequency f) tend to concentrate energy in horizontal motions that change rapidly with depth, making shear-dominated fields a hallmark of low-frequency wave regimes.

Conversely, when $\omega \approx N$, $k_h \gg k_z$ and the particle motion becomes primarily vertical, enhancing isopycnal displacement and thus the strain $\partial\xi/\partial z$ (i.e., significant vertical displacements of isopycnals). It results that the wave propagates with a nearly vertical beam and the wave field varies slowly with depth. For this condition, although the vertical structure of the wave is broad (i.e., fewer oscillations along z), the amplitude of vertical displacements is large. As a result, the isopycnals experience stronger stretching and compression, leading to enhanced strain energy. This explains why internal waves at high frequencies, despite their low vertical wavenumber, contribute disproportionately to the strain variance. The enhanced vertical motion associated with high-frequency waves increases the spatial variability of ξ, and thus the observed strain, even if ∂ξ/∂z is not large in the sinusoidal sense. In real oceanic spectra, high-frequency components carry more energy in vertical displacement, making the strain-dominated regime a hallmark of high-frequency wavefields.

A propagation angle of an internal wave ray can be determined using the dispersion relation:

https://doi.org/10.5194/egusphere-2025-4762
Preprint. Discussion started: 9 October 2025

$$\frac{{k_z}^2}{{k_x}^2+{k_y}^2} = \frac{N^2-\omega^2}{\omega^2-f^2}; \quad (8)$$

thus,

$$tan^2\alpha = \frac{N^2-\omega^2}{\omega^2-f^2}. \quad (9)$$

From Equation (9), the angle of the wave trajectory (i.e., the beam angle α) relative to the horizontal can be determined. The angle α describes a cone of propagation that supports the wave:

$$\alpha = tan^{-1}\sqrt{\frac{N^2-\omega^2}{\omega^2-f^2}}. \quad (10)$$

The wave energy propagates with the group velocity $\boldsymbol{c}_g$, perpendicular to the wave direction $\boldsymbol{k}$, at an angle $\beta = 90° - \alpha$. For R_ω it is possible to derive the following expression (see Kunze et al,. 2006; Ijichi and Hibiya, 2015):

$$R_\omega = \frac{\langle V_z^2\rangle}{\langle \xi_z^2\rangle N^2} = \frac{\omega^2+f^2}{\omega^2-f^2} \simeq 1 + \frac{2f^2k_z^2}{N^2k_h^2}, \quad (11)$$

from which we estimate a local value of ω in the water-column, given $N(z)$ and the local f, that we assume representative of a certain regional extent on the horizontal. From ω we can estimate β perpendicular to α. The relation between R_ω, ω and β will be exploited later in our study to associate the beam angle with R_ω value and compare it with the bathymetrical slope to infer propagation insights. Equation (10), along with the physical interpretation of Equation (7), highlights that the wave geometry (i.e., the ratio k_z^2/k_h^2) dominates the shear-strain dynamics: for $k_z \gg k_h$ we have high shear and R_ω values, and for $k_h \gg k_z$ high strain values and low R_ω. In other words, high R_ω values correspond to low-frequency, shear-dominated conditions, while low R_ω indicates high-frequency, strain-dominated fields.

A growing body of evidence shows that turbulent mixing is significantly enhanced in regions of rough bottom topography and sloping boundaries (Polzin et al., 1997; Ledwell et al., 2000; Kunze et al., 2006; Ferrari et al., 2016; Mashayek et al., 2017). Internal wave interactions with these features

https://doi.org/10.5194/egusphere-2025-4762
Preprint. Discussion started: 9 October 2025

can lead to reflection, scattering, and energy transfer toward higher vertical wavenumbers, increasing the likelihood of wave breaking and dissipation (Nash et al., 2004; Legg & Adcroft, 2003; Musgrave et al., 2022). In addition to tidal processes, geostrophic flows impinging on small-scale topography generate broadband internal waves that can radiate and dissipate energy locally, contributing to abyssal mixing (Nikurashin & Ferrari, 2010a, 2010b). These mechanisms, collectively, explain much of the spatial variability in observed mixing rates and highlight the importance of accurately representing topographic interactions in ocean mixing parameterizations.

When an internal wave encounters a rough topography, its propagation is disturbed, promoting scattering, reflection, or the generation of higher-frequency waves. This tends to break down low-frequency, large-scale wave structures and shift spectral energy toward higher vertical wavenumbers.

Since strain is associated with large vertical displacements, characteristic of high-frequency waves, this shift leads to a systematic decrease of the shear-to-strain variance ratio R_ω in rougher regions, as documented in Kunze et al. (2006), where departures from the canonical Garrett–Munk spectrum were observed in high-roughness environments. As a result, areas of high roughness typically exhibit lower R_ω, indicating increased strain. In contrast, smoother topographic regions preserve the lower-frequency shear-dominated character, yielding higher R_ω.

In our investigation of the impact of bathymetry on R_ω, we analyze the KM3NeT hydrological stations in relation to bathymetric features such as slope and topographic roughness, calculated using the GEBCO gridded data (https://www.gebco.net) over the Ionian Sea area, at 15 arc-second intervals. In particular, slopes are estimated between the hydrological cast position and the points located apart in the eight cardinal directions around, then the average is retained. A distance of 10 km between the two points is chosen to avoid overestimation of the topographic slope, due to the presence of small bathymetric features. Topographic roughness is calculated from the variance of the bathymetry over the same neighboring area (i.e., 20-by-20 square kilometers).

3 Results

To investigate the influence of bottom topography on internal wave shear-to-strain ratio from Equation (6), our dataset is bin-averaged every 80 m, from bottom to surface. From the first upward segment of 640 m we obtain values at the center of the segment (i.e. 320 m from bottom), and the associated first binned value is available into bin 4, centered at 360 m from bottom. We stop then at bin 12 (centered 920 m from the bottom). By doing this, we consider 8 bins of 80 m (Figure 1b).

Results show that most of the near-bottom values of R_ω are larger than the canonical value of 3, given by the GM model (Figures 1 and 2a; Supplementary Table S1). Smaller values, from 1.01 to 10, are generally observed in the shelf break regions, as well as at some deep stations (Figures 1 and 2a; Supplementary Table S1), or close to the Malta escarpment, where mesoscale bottom meandering and vortical structures occur (Sparnocchia et a., 2011; Rubino et al., 2012). For deep, offshore casts, estimations show large values. An increase of shear-to-strain ratio is evident in the western part of the abyssal plain, between 2000 and 3000 m depth, i.e., along the offshore portion of the three cross-shore transects T1, T2, and T3 (Figure 1a and 2a). Here, R_ω shows values between ~10 and ~30 (Figures 1 and 2a; Supplementary Table S1).

https://doi.org/10.5194/egusphere-2025-4762
Preprint. Discussion started: 9 October 2025

R_ω values are then compared with the local bathymetric roughness, i.e., the logarithm of the variance of seafloor elevation (Figures 2a,b). In general, it results that regions with higher roughness show lower R_ω, suggesting, for those regions, a shift toward higher-frequency energy and enhanced vertical displacement (i.e., strain). High values of bottom roughness are distributed along the eastern and northern shelf; a smoother bathymetry is recognized in the abyssal plain. Correspondingly, R_ω displays lower values (<10) in areas of high roughness, while offshore regions are associated with higher values (>10). By plotting R_ω against bathymetric slope and roughness (Figure 2c), we find that although a linear relationship is difficult to establish, an interesting pattern emerges: increased roughness appears to reduce the dispersion of R_ω. This effect could also be attributed to the bathymetric slope, as slope and roughness are correlated, with steeper zones leading to greater variance in elevation. We hypothesize that this pattern indicates waves being constrained toward higher frequency bands by the roughness.

Indeed, further analyses show how the increasing R_ω corresponds to decreasing frequency and flatter beam angles (i.e., more horizontal propagation), while low R_ω indicates steeper beams and higher frequencies (Figure 3a). The vertical line and shaded area in Figure 3a highlight the mean and observed range of R_ω in our dataset, contextualizing the frequencies and angles involved. This framework sets the stage for comparing beam angles with local bathymetric slopes. A Δ-slope is inferred as the difference between the bulk beam angle in Equation 10 and the bathymetry slope. This angle controls the reflection regime: near-critical reflection (Δ-slope $\approx 0°$) concentrates energy in horizontal shear, while supercritical conditions (Δ-slope $> 0°$) promote upward-propagating waves and stronger vertical displacements (strain) (Musgrave et al., 2022). Once scattered through this quantity, a clear pattern appears, i.e., R_ω is clearly related to Δ-slope (Figure 3b). Higher R_ω values correspond to smaller angle differences, while lower R_ω values are associated with steeper conditions. This indicates a shift in frequency content, illustrated by the associated ω-distribution (Figure. 3c), with frequencies increasing as Δ-slope grows. Additionally, roughness appears to constrain the dynamical range of R_ω dispersion. This suggests a critical threshold where high frequencies and smaller scales begin to dominate over shear.

By organizing the shear and strain spectra into bins of roughness and Δ-slope to identify whether specific bandwidths are affected, one might expect enhanced signals at larger vertical scales (≈300 m) or smaller scales (≈100 m), depending on the preferential frequency content potentially enhanced by the bathymetric features. The resulting spectra (Figure 4a) show that strain variance increases at high vertical wavenumbers (small vertical scales) in those regions characterized by elevated roughness, while shear variance diminishes at low wavenumbers, reflecting a redistribution of energy across scales. Indeed, shear spectra under rougher conditions (blue spectra in Figure 4a) appear flatter in the lower wavenumber band compared to smoother regions. Intermediate roughness levels (green spectra in Figure 4a) show increased energy around vertical scales of 64 m, potentially indicating enhanced energy distribution at shorter scales. Strain spectra exhibit a distinct pattern for strong roughness, with higher energy levels compared to other bins. These observations suggest that increasing roughness reduces energy distribution at larger scales (shear lower band) while enhancing strain variance contributions at smaller scales (upper band).

To isolate the influence of slope geometry, we use the beam-to-slope angle difference Δ-slope. The shear spectra in Figure 4b show a clear dependence on Δ-slope. Indeed, higher R_ω values correspond to smaller angle differences, while lower R_ω values are associated with steeper conditions. This indicates a shift in frequency content, with frequencies increasing as Δ-slope grows. Spectra in Figure 4b support what we observed in Figure 3, suggesting a critical threshold where high frequencies and

https://doi.org/10.5194/egusphere-2025-4762
Preprint. Discussion started: 9 October 2025

smaller scales begin to dominate over shear. This interpretation is further confirmed by the patterns observed in Figure 5: as Δ-slope approaches 0, lower frequencies become dominant, indicating more horizontal motion. This is associated with increased shear and a higher prevalence of critical Richardson instability events (Figure 5a,b). The deviation from the GM model is evident in the shear ratio, with values exceeding 8–10 times the model (Figure 5c,d), while the strain consistently remains below the GM model's predictions (Figure e,f), and vice-versa.

Regarding dissipation or diffusion rates of turbulent kinetic energy, we present their associated scatterplot and geographical distributions in Figure 6. Spatial pattern of diapycnal diffusivity (K_{iw}; Figure 6f) shows that our estimates are close to the typical "low" observed ocean values of 10^{-5} or below (10^{-6}) (Munk, 1966; Kunze and Toole, 1997; Polzin et al., 1997), between 1000 and 2500 m depth, on the northern part of the area (e.g., stations NK30, NK31 of transect T1 and stations NK26, NK25, and NK24 of transect T2; Figures 1a; Supplementary Table S1). Intensified area corresponds to roughest zones with values spanning above 5 10^{-5} up to closer to 10^{-4} (NK32, NK21, NK22, NK27, NK13, 11 NK17, NK6; Figures 1a; Supplementary Table S1). In the abyssal layer, the function F(R_ω) in Eq. (3), in becoming smaller than 1 for large values of R_ω, contributes to inhibit the terms of the parameterization (see Data and methods). In this layer IW mixing is expected to be weak. Although ε_{iw} and K_{iw} obviously depend on R_ω, scatter plots in Fig 6a-d show how intense values of dissipation or diffusion rates are coherently distributed along Δ-slope values.

4 Discussions and conclusions

Mixing in the ocean can be triggered by the combination of boundary constraints and hydrographic conditions (Marotzke and Scott, 1999; Kuhlbrodt, 2008), and it is concentrated above seamounts, mid-ocean ridges, and along/cross strong ocean currents (Polzin et al., 1997; Ledwell et al., 2000). In these conditions, diapycnal mixing contributes to transfer and redistribute water masses and heat throughout the deep ocean (Polzin et al., 1997; Ledwell et al., 2000; Marotzke and Scott, 1999; Levitus et al., 2000; Artale et al., 2018). By increasing the potential energy within a stratified fluid, and thus by raising the water mass center on a larger time and spatial scale, diapycnal mixing maintains the long-term baroclinic balance of the water column (Wunsch, C., & Ferrari, 2004; Munk and Wunsch, 1998; Iudicone et al., 2003), thus contributing to the general ventilation of ocean basins. Investigations on turbulent vertical mixing in the deep sea revealed that abyssal circulation and the related dynamical effects of deep upwelling are more complex than what was envisioned during the twentieth century (Stommel and Arons, 1959; Polzin et al., 1997).

Our analysis in the Ionian Sea contributes to the investigation of the IW mixing, as described by Kunze et al. (2006). We focused on hydrological stations where we took advantage of synchronous LADCP and CTD profiles from which we infer regional values of the near-bottom ratio between shear and strain variances (R_ω). Values for R_ω are necessary for deriving both dissipation rate of turbulent kinetic energy and diapycnal diffusivity (i.e., ε_{iw} and K_{iw}, respectively). Our goal, in particular, was to quantitatively assess the spatial patterns of shear-to-strain ratio to highlight the role of morpho-bathymetric features in enhancing dissipation and diffusion rates, in terms of depth, slope, and roughness.

We found a general relation between bottom depth and shear-to-strain variance ratio (R_ω), which tends to increase from the shelf break to the abyss: large (small) value of R_ω is found over small (large) topographic slope and/or low (high) roughness of the seafloor, consistent with the hypothesis that gentle (steep) slopes and/or low (high) roughness would generate low (high) frequency internal

https://doi.org/10.5194/egusphere-2025-4762
Preprint. Discussion started: 9 October 2025

waves, leading to the increase in the shear (strain) contribution. In particular, for the northwest group of stations (i.e., the shelf-to-plain transects T1, T2, and T3; Figure 1a), we found coherent trends of R_ω, which co-varies with depth, slope, and roughness. Among those stations, high values of R_ω tend to inhibit both ε_{iw} and K_{iw}.

Our observations bring to hypothesized that, in rougher conditions, the intensified energy cascade and dissipation related to the increase in local shear, tend to break down coherent vertical displacements associated with IWs. This can result in a suppression of the strain spectra in these rougher areas. The imbalance observed (enhancement of shear variance and lower strain variance, with respect of the trend observed for the other roughness cases) reflects a wave field that is more turbulent and less coherent (Chinn et al, 2016).

Although in abyssal waters (i.e., deeper than 3000 m), specific stations of transect T4 (e.g., from Station NK6 to Station 11; Figure 1a) show a behavior similar to the one observed in the shelf-to-plain transects: R_ω increases with distance from the shelf break, starting from $R_\omega \sim 10$, although we are in abyssal waters. We notice, however, that those abyssal stations of Transect 4 that show low values of R_ω (i.e., values we expect in shallow areas) are close to the topographic constraints of the Malta Escarpment (Figure 1a), where energetic mesoscale meandering features and vortical structures at the bottom, were observed (Rubino et al., 2012; Meccia et al., 2015). These low values of shear-to-strain ratio may be due to the eventual mesoscale eddy–internal wave coupling that would represent a sink of eddy energy and then a source of IW energy (Polzin, 2010; Takahashi et al., 2021). These abyssal stations in Transect 4 may therefore represent those particular, "nontraditional" cases (Gerkema and Shrira, 2005) where deep mesoscale activity is able to trigger diapycnal mixing by breaking of IWs.

Kunze et al. (2006) suggested that the lack of reflectors in the water column at deep locations could lead to an overestimation of the shear variance, reflected ultimately in strong values of R_ω. However, the in-situ spectra we analyzed do not indicate such a contamination.

In particular, we observe that the bottom layer of the eastern abyssal stations is prone to double-diffusion processes, which may not make our analysis reliable: stations NK17, 12, and 13 (in transect T4), station 25 (Transect 2), and stations 32 and 34 (Transect 1) are those that show more than 60% of the near-bottom water column, with a Turner angle $-90° < Tu < -45°$ (i.e., diffusive convection regime) and $45° < Tu < 90°$ (salt fingering regime), and a Richardson number $Ri < 0.25$ (Miles, 1961; Ruddick, 1983; Thorpe, 2005). An additional analysis of the density ratio Rρ (not shown) indicates that only a few thin layers fall within the "active" ranges typically used in double-diffusion parameterizations (0.5–1 for diffusive convection and 1–3 for salt fingering). This suggests that, while double-diffusive processes may occur locally, their influence on the overall analysis is likely limited.

Baroclinic tide and lee wave generation by tidal and geostrophic flows impinging on rough topography are among the most significant sources of IW energy for the deep ocean (Egbert and Ray, 2000; Garrett and St. Laurent, 2002; Cavaliere et al., 2021; La Forgia et al., 2021). Our results reinforce the concept of IW generation from the interaction between deep, geostrophic currents and the topographic constraint and roughness, which in turn may cause local breaking processes. In assessing an actual, systematic morpho-bathymetric characterization of the shear and strain variances, we also highlight horizontal gradients of dissipation rate and diapycnal diffusivity we observe. This results in horizontal gradients of vertical mixing that affect thermohaline gradients that, in turn, may trigger additional components for the bottom ocean circulation (Jones and Abernathey, 2019).

Finally, our analysis aims to provide useful insights for ocean circulation models, which are often too sensitive to vertical eddy diffusivity and are largely affected by inaccuracy at deep layers (Gargett and Holloway, 1982; Wright and Stocker, 1992). In particular, the large variability of the shear-to-strain ratio we found, may help the parametrization of mixing that should capture the

https://doi.org/10.5194/egusphere-2025-4762
Preprint. Discussion started: 9 October 2025

additional abyssal flow from the inclusion of wave–driven mixing (Simmons et al., 2004; Saenko and Merryfield, 2005; Oka and Niwa, 2013; Melet et al., 2014; De Lavergne et al., 2016).

5 Conflict of Interest

The authors declare that the research was conducted in the absence of any commercial or financial relationships that could be construed as a potential conflict of interest.

6 Author Contributions

FF, VA, and FK delineated, supervised the study. SS, MB, and FF collected the data. SS and FK processed and analyzed the CTD and LADCP data. FK, SS, VA, DC, and FF contributed with resources, analyzed the data and wrote the manuscript.

7 Funding

This work was partially supported by EMODnet (European Marine Observation and Data Network Physics), the Copernicus Climate Change Service (C3S) project, and the Flagship Project RITMARE (The Italian Research for the Sea), coordinated by the Italian National Research Council and funded by the Italian Ministry of Education, University and Research.

8 Acknowledgments

Data were collected in the framework of the project ‘‘Specific Support Action for the Design Study for a Deep-Sea Facility in the Mediterranean for Neutrino Astronomy and Associated Sciences’’ (KM3NeT), EU contract no. 011937. We thank Daniele Iudicone, Manuel Bensi, and Enrico Zambianchi for the insightful discussion at the initial stage of the investigation.

9 Data and Code Availability

Data are available on Sea Scientific Open Data Publication (SEANOE), https://www.seanoe.org/preview/108742?token=NkpdOxO5966RjZ--Rqdw1c0dCZ-6iGSW
Codes that were used for this analysis are available at https://zenodo.org/records/17170422 (DOI: 10.5281/zenodo.17170421)

https://doi.org/10.5194/egusphere-2025-4762
Preprint. Discussion started: 9 October 2025

592 **Figures**

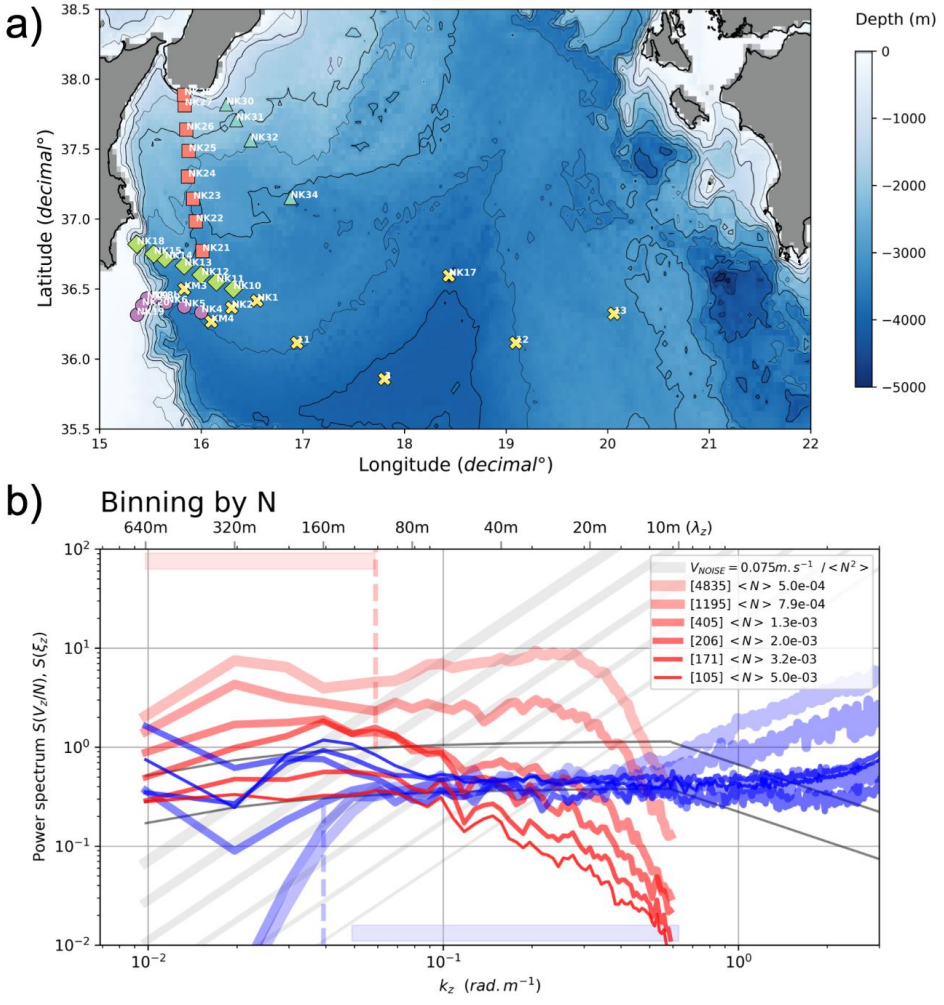

593

594 **Figure 1. a)** The Mediterranean Sea bathymetry and the main regional features that are discussed
595 within the text; LADCP-CTD casts are grouped in four main hydrological transects: three shelf-to-
596 plain transects, i.e., T1 (▲), T2 (■), and T3 (♦) and one abyssal transect T4(✕). **b)** Buoyancy-
597 normalized shear (red) and strain (blue) wavenumber spectra, with their associated GM model (upper
598 black line: shear; lower black line: strain). Spectra are averaged by bins of stratification (thick to thin,
599 from weak to higher stratification). Number of spectra by bins, with the average N of the bin are
600 reported in legend. Shear noise spectra associated with a noise velocity of 0.075 m/s are indicated in
601 gray (thickness indicates its association to the N bins). Instrumental wavenumber limits are indicated
602 with the vertical dotted lines: upper limit of $2\pi/128\ rad \cdot m^{-1}$ for shear due to noise contamination;
603 lower limit of $2\pi/160\ rad \cdot m^{-1}$ for strain to filter the large-scale background stratification. Retained
604 wavenumber bandwidths for integration are indicated with the shaded ranges on top and bottom (640-
605 107 m for shear; 128-10 m for strain).
606

https://doi.org/10.5194/egusphere-2025-4762
Preprint. Discussion started: 9 October 2025

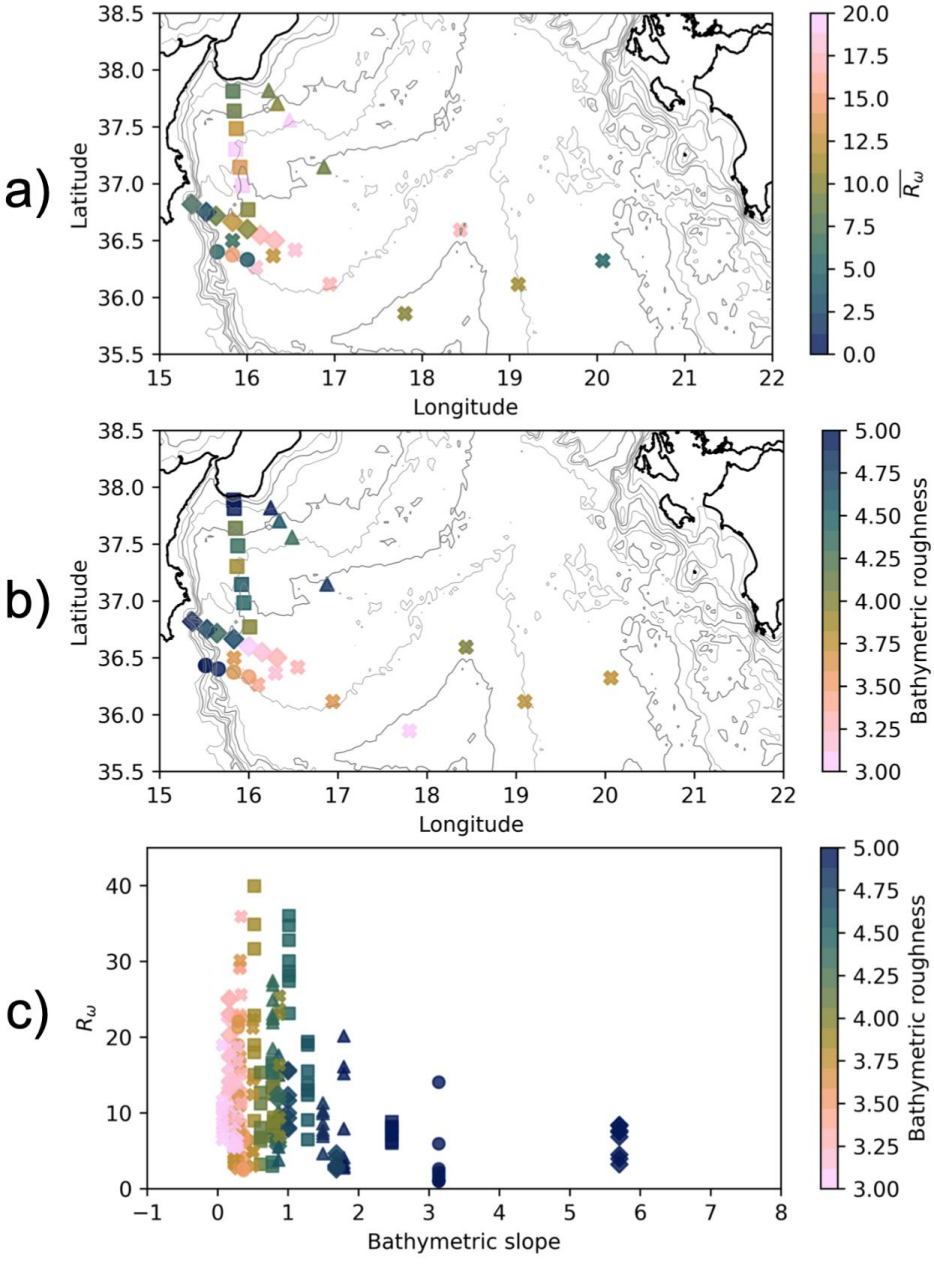

Figure 2. **a)** Shear-to-strain ratio R_ω at the bottom of the LADCP-CTD profiles, averaged from bins of 80m in the layer 360-920m distant from the bottom; low (high) values of R_ω correspond to high- (low-) frequency, strain-dominated (shear-dominated) regimes. **b)** Bottom roughness (log10 of var(z)) over the study area. **c)** Scatterplot of R_ω as a function of bathymetric slope (x-axis), and roughness (z-axis, in color).

https://doi.org/10.5194/egusphere-2025-4762
Preprint. Discussion started: 9 October 2025

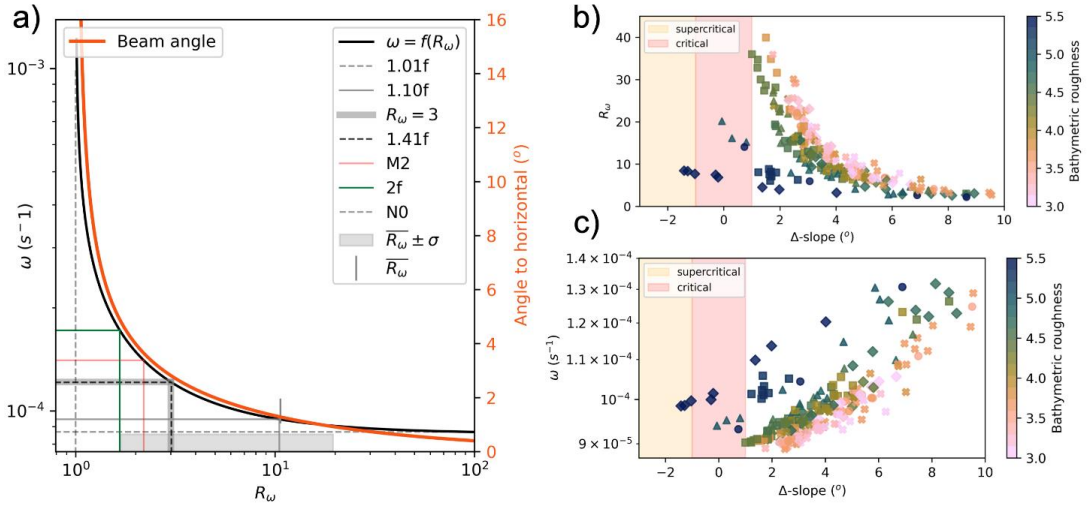

Figure 3. a) Correspondence between R_ω and ω (black), and the beam angle associated with R_ω (orange), computed at the average latitude of the study (36.75ºN). Typical values, from high to low R_ω, are reported. The average R_ω value of our study is indicated with the vertical line marker, and its distribution range is indicated by the gray area. **b)** Distributions of R_ω and **c)** ω in the layer 360-920 m distant from bottom, in function of the difference between the associated beam angle and the bathymetry slope (Δ-slope). Roughness is indicated through the z-axis (in color). Higher values on the x-axis indicate a beam angle steeper, relative to the bathymetry slope, while lower values indicate a beam aligning with the slope. The critical range where the alignment is close to be parallel to the slope is arbitrarily marked by the shaded red area from -1 to 1 degrees, out of which a supercritical range is indicated in orange.

https://doi.org/10.5194/egusphere-2025-4762
Preprint. Discussion started: 9 October 2025

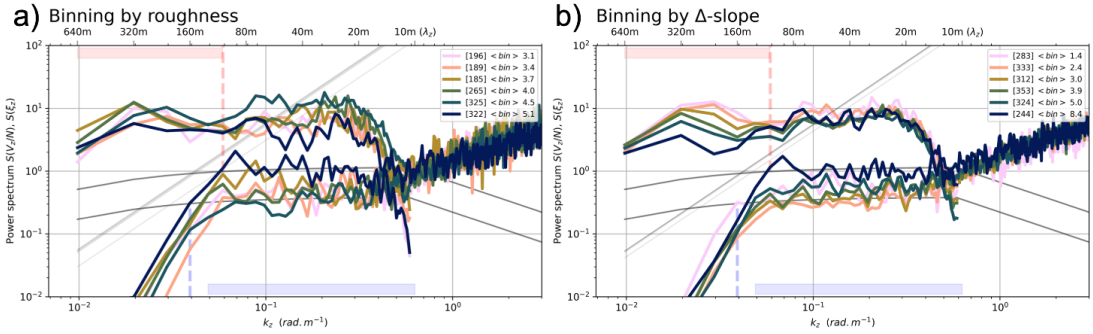

Figure 4. Buoyancy-normalized shear **(top)** and strain **(bottom)** wavenumber spectra, with their associated GM model (upper black: shear; lower black: strain). Spectra are averaged by bins of roughness (**a**), and by bins of the difference between the beam angle and the bathymetry slope angle (**b**). For both (a) and (b) number of spectra found by bins and the average bin value are reported in legend. Shear noise spectra associated with a noise velocity of 0.075 m/s are indicated in gray (thickness indicates its association to the N bins). Instrumental wavenumber limits are indicated with the vertical dotted lines: upper limit of $2\pi/128\ rad \cdot m^{-1}$ for shear due to noise contamination; lower limit of $2\pi/160\ rad \cdot m^{-1}$ for strain to filter the large-scale background stratification. Retained wavenumber bandwidths for integration are indicated with the shaded ranges on top and bottom (640-107 m for shear; 128-10 m for strain).

https://doi.org/10.5194/egusphere-2025-4762
Preprint. Discussion started: 9 October 2025

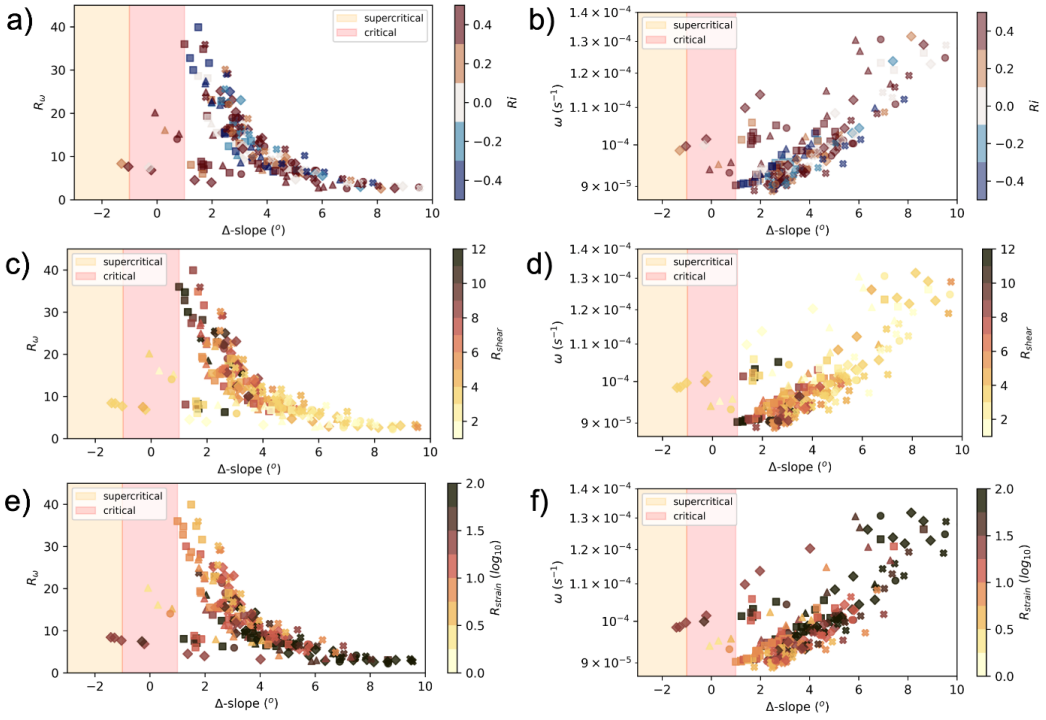

Figure 5. Distributions of R_ω (**left**) and ω (**right**) in the layer 360-920m distant from the bottom, in function of the difference between the associated beam angle and the bathymetry slope angle. *Z*-axis is used to indicate **(a,b)** a bulk Richardson number, **(c,d)** the shear-to-shear-GM ratio, **(e,f)** the strain-to-strain-GM ratio. Higher values on the *x*-axis indicate a beam angle steeper, relative to the bathymetry slope, while lower values indicate a beam aligning with the slope. The critical range where the alignment is close to be parallel to the slope is arbitrarily marked by the shaded red area from -1 to 1 degrees, out of which a supercritical range is indicated in orange.

https://doi.org/10.5194/egusphere-2025-4762
Preprint. Discussion started: 9 October 2025

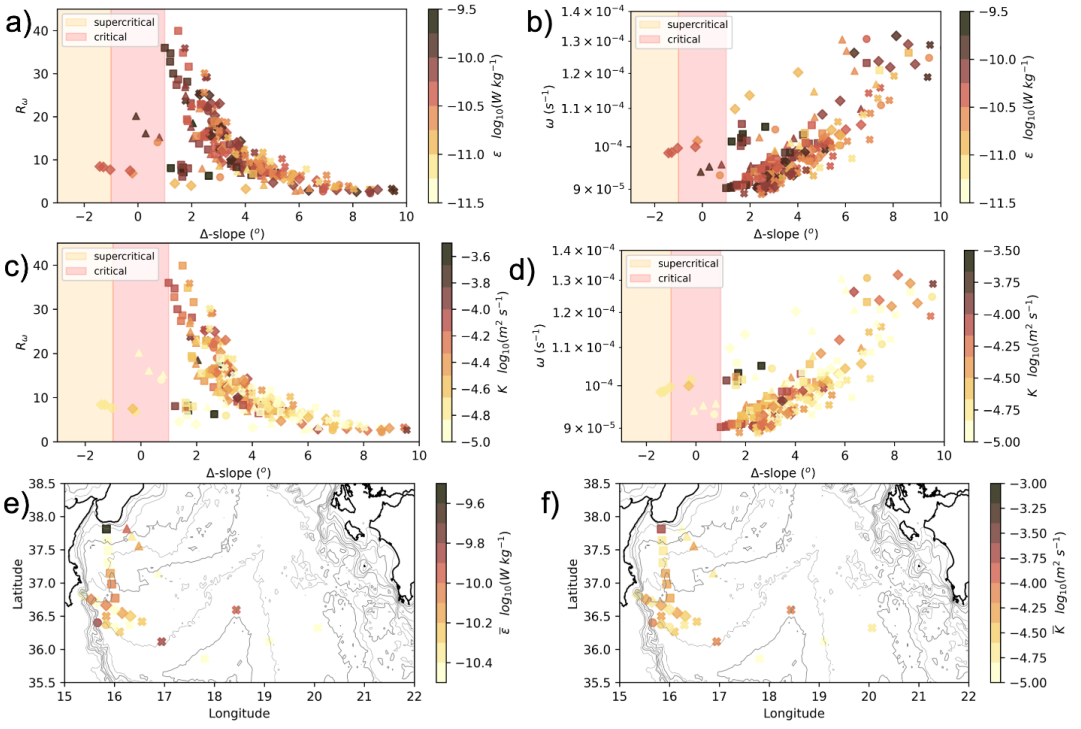

Figure 6. Distributions of R_ω and ω in the layer 360-920 m distant from the bottom, in function of the difference between the associated beam angle and the bathymetry slope angle. Z-axis is used to indicate the turbulent kinetic energy dissipation rate in log10 of $W\ kg^{-1}$**(a,b)** and diffusion rates in log10 of $m^2\ s^{-1}$ **(c,d)** resulting from the parametrizations. Their respective averages in bins of 80m in the layer 360-920m distant from the bottom are reported over the geographical map of the Ionian Sea (dissipation in **e)**, diffusion in **f)**).

https://doi.org/10.5194/egusphere-2025-4762
Preprint. Discussion started: 9 October 2025

10 References

Artale, V., Calmanti, S., Malanotte-Rizzoli, P., Pisacane, G., Rupolo, V., & Tsimplis, M. (2006). The Atlantic and Mediterranean Sea as connected systems. In *Developments in Earth and Environmental Sciences* (Vol. 4, pp. 283-323). Elsevier.

Artale, V., Falcini, F., Marullo, S., Bensi, M., Kokoszka, F., Iudicone, D., & Rubino, A. (2018). Linking mixing processes and climate variability to the heat content distribution of the Eastern Mediterranean abyss. *Scientific reports*, *8*(1), 1-10.

Bellacicco, M., Anagnostou, C., Falcini, F., Rinaldi, E., Tripsanas, K., & Salusti, E. (2016). The 1987 Aegean dense water formation: A streamtube investigation by comparing theoretical model results, satellite, field, and numerical data with contourite distribution. *Marine Geology*, 375, 120-133.

Bensi, M., Cardin, V., Rubino, A., Notarstefano, G., & Poulain, P. M. (2013b). Effects of winter convection on the deep layer of the Southern Adriatic Sea in 2012. *Journal of Geophysical Research: Oceans*, *118*(11), 6064-6075.

Bensi, M., Rubino, A., Cardin, V., Hainbucher, D., & Mancero-Mosquera, I. (2013a). Structure and variability of the abyssal water masses in the Ionian Sea in the period 2003-2010. *Journal of Geophysical Research: Oceans*, *118*(2), 931-943.

Béranger, K., Mortier, L., Gasparini, G. P., Gervasio, L., Astraldi, M., & Crépon, M. (2004). The dynamics of the Sicily Strait: a comprehensive study from observations and models. *Deep Sea Research Part II: Topical Studies in Oceanography*, 51(4-5), 411-440.

Bergamasco, A., & Malanotte-Rizzoli, P. (2010). The circulation of the Mediterranean Sea: a historical review of experimental investigations. *Advances in Oceanography and Limnology*, 1(1), 11-28.

Bindoff, N. L., Willebrand, J., Artale, V., Cazenave, A., Gregory, J. M., Gulev, S., ... & Woodworth, P. (2007). Observations: oceanic climate change and sea level. *Climate Change 2007: The Physical Science Basis*, eds Solomon S, et al. (Cambridge Univ Press, Cambridge, UK), pp 747–845.

Borghini, M., Falcini, F., Kokoszka, F., Sparnocchia S. (2025). CTD and LADCP data from the KM3NET cruise, Ionian Sea, July 2007. *SEANOE* (https://www.seanoe.org/preview/108742?token=NkpdOxO5966RjZ--Rqdw1c0dCZ-6iGSW).

Cairns, J. L., & Williams, G. O. (1976). Internal wave observations from a midwater float, 2. *Journal of Geophysical Research*, *81*(12), 1943-1950.

Cavaliere, D., La Forgia, G., Adduce, C., Alpers, W., Martorelli, E., & Falcini, F. (2021). Breaking location of Internal Solitary Waves over a sloping seabed. *Journal of Geophysical Research: Oceans*, *126(2),* e2020JC016669.

Chinn, B. S., Girton, J. B., & Alford, M. H. (2016). The impact of observed variations in the shear-to-strain ratio of internal waves on inferred turbulent diffusivities. *Journal of Physical Oceanography*, *46*(11), 3299-3320.

De Lavergne, C., Madec, G., Le Sommer, J., Nurser, A. G., & Naveira Garabato, A. C. (2016). The impact of a variable mixing efficiency on the abyssal overturning. *Journal of Physical Oceanography*, *46*(2), 663-681.

https://doi.org/10.5194/egusphere-2025-4762
Preprint. Discussion started: 9 October 2025

774 Dematteis, G., Le Boyer, A., Pollmann, F., Polzin, K. L., Alford, M. H., Whalen, C. B., & Lvov, Y.
775 V. (2024). Interacting internal waves explain global patterns of interior ocean mixing. *Nature*
776 *Communications*, *15*(1), 7468.

777 Egbert, G. D., & Ray, R. D. (2000). Significant dissipation of tidal energy in the deep ocean inferred
778 from satellite altimeter data. *Nature*, *405*(6788), 775-778.

779 Ferrari, R. (2014). What goes down must come up. *Nature*, *513*(7517), 179-180.

780 Ferrari, R., and Wunsch, C. (2009) Ocean Circulation Kinetic Energy: Reservoirs, Sources, and Sinks.
781 Annual Review of Fluid Mechanics, 41, 253–282.
782 https://doi.org/10.1146/annurev.fluid.40.111406.102139

783 Ferrari, R., Mashayek, A., McDougall, T. J., Nikurashin, M., & Campin, J. M. (2016). Turning ocean
784 mixing upside down. *Journal of Physical Oceanography*, *46*(7), 2239-2261.

785 Ferron, B., Kokoszka, F., Mercier, H., & Lherminier, P. (2014). Dissipation rate estimates from
786 microstructure and finescale internal wave observations along the A25 Greenland–Portugal OVIDE
787 line. *Journal of Atmospheric and Oceanic Technology*, 31(11), 2530-2543.

788 Ferron, B., Kokoszka, F., Mercier, H., Lherminier, P., Huck, T., Rios, A., & Thierry, V. (2016).
789 Variability of the turbulent kinetic energy dissipation along the A25 Greenland–Portugal transect
790 repeated from 2002 to 2012. *Journal of Physical Oceanography*, 46(7), 1989-2003.

791 Ferron, B., Bouruet Aubertot, P., Cuypers, Y., Schroeder, K., & Borghini, M. (2017). How important
792 are diapycnal mixing and geothermal heating for the deep circulation of the Western Mediterranean?.
793 *Geophysical Research Letters*, 44(15), 7845-7854.

794 Gačić, M., Borzelli, G. E., Civitarese, G., Cardin, V., & Yari, S. (2010). Can internal processes sustain
795 reversals of the ocean upper circulation? The Ionian Sea example. *Geophysical research letters*,
796 *37*(9).

797 Gargett, A. E. (1990). Do we really know how to scale the turbulent kinetic energy dissipation rate ε
798 due to breaking of oceanic internal waves?. *Journal of Geophysical Research: Oceans*, *95*(C9),
799 15971-15974.

800 Gargett, A. E., & Holloway, G. (1992). Sensitivity of the GFDL ocean model to different diffusivities
801 for heat and salt. *Journal of physical oceanography*, *22*(10), 1158-1177.

802 Garrett, C., & Kunze, E. (2007). Internal tide generation in the deep ocean. *Annu. Rev. Fluid Mech.*,
803 *39*, 57-87.

804 Garrett, C., & Laurent, L. S. (2002). Aspects of deep ocean mixing. *Journal of oceanography*, *58*(1),
805 11-24.

806 Garrett, C., & Munk, W. (1975). Space-time scales of internal waves: A progress report. *Journal of*
807 *Geophysical Research*, *80*(3), 291-297.

808 Gerkema, T., & Shrira, V. I. (2005). Near-inertial waves on the "nontraditional" β plane. *Journal of*
809 *Geophysical Research: Oceans*, *110*(C1).

https://doi.org/10.5194/egusphere-2025-4762
Preprint. Discussion started: 9 October 2025

Gerkema, T., & Zimmerman, J. T. F. (2008). *An introduction to internal waves*. Lecture Notes, Royal NIOZ, Texel, 207.

Henyey, F. S., Wright, J., & Flatté, S. M. (1986). Energy and action flow through the internal wave field: An eikonal approach. *Journal of Geophysical Research: Oceans*, *91*(C7), 8487-8495.

Holte, J., & Straneo, F. (2017). Seasonal overturning of the Labrador Sea as observed by Argo floats. *Journal of Physical Oceanography*, 47(10), 2531-2543.

Ijichi, T., & Hibiya, T. (2015). Frequency-based correction of finescale parameterization of turbulent dissipation in the deep ocean. *Journal of Atmospheric and Oceanic Technology*, 32(8), 1526-1535.

Ijichi, T., & Hibiya, T. (2017). Eikonal calculations for energy transfer in the deep-ocean internal wave field near mixing hotspots. *Journal of Physical Oceanography*, 47(1), 199-210.

Iudicone, D., Buongiorno Nardelli, B., Santoleri, R., & Marullo, S. (2003). Distribution and mixing of intermediate water masses in the Channel of Sicily (Mediterranean Sea). *Journal of Geophysical Research: Oceans*, 108(C9).

Jones, C. S., & Abernathey, R. P. (2019). Isopycnal mixing controls deep ocean ventilation. *Geophysical Research Letters*, *46*(22), 13144-13151.

Katz, U. F. (2006). KM3NeT: Towards a km3 Mediterranean neutrino telescope. *Nuclear Instruments and Methods in Physics Research Section A: Accelerators, Spectrometers, Detectors and Associated Equipment*, 567(2), 457-461.

Kokoszka, F. (2025). Supporting code, fszk/internal-waves-finescale: Finescale parameterization shear/strain GM (v1.0.0). *Zenodo*. https://doi.org/10.5281/zenodo.17170422

Kuhlbrodt, T. (2008). On Sandström's inferences from his tank experiments: a hundred years later. *Tellus A: Dynamic Meteorology and Oceanography*, *60*(5), 819-836.

Kunze, E., & Toole, J. M. (1997). Tidally driven vorticity, diurnal shear, and turbulence atop Fieberling Seamount. *Journal of Physical Oceanography*, 27(12), 2663-2693.

Kunze, E., Firing, E., Hummon, J. M., Chereskin, T. K., & Thurnherr, A. M. (2006). Global abyssal mixing inferred from lowered ADCP shear and CTD strain profiles. *Journal of Physical Oceanography*, *36*(8), 1553-1576.

La Forgia, G., Cavaliere, D., Adduce, C., Falcini, F. (2021). Mixing efficiency for breaking internal solitary waves. *Journal of Geophysical Research: Oceans*, 2021JC017275-TR (in revision).

Ledwell, J. R., Montgomery, E. T., Polzin, K. L., Laurent, L. S., Schmitt, R. W., & Toole, J. M. (2000). Evidence for enhanced mixing over rough topography in the abyssal ocean. *Nature*, *403*(6766), 179-182.

Legg, S., & Adcroft, A. (2003). Internal wave breaking at concave and convex continental slopes. *Journal of Physical Oceanography*, *33*(11), 2224-2246.

Levitus, S., Antonov, J. I., Boyer, T. P., & Stephens, C. (2000). Warming of the world ocean. *Science*, *287*(5461), 2225-2229.

https://doi.org/10.5194/egusphere-2025-4762
Preprint. Discussion started: 9 October 2025

MacKinnon, J. A., et al. (2017). Climate Process Team on Internal Wave–Driven Ocean Mixing. Bulletin of the American Meteorological Society, 98(11), 2429–2454. https://doi.org/10.1175/BAMS-D-16-0030.1

Malanotte-Rizzoli, P., & Hecht, A. (1988). Large-scale properties of the eastern mediterranean-A review. *Oceanologica Acta*, 11(4), 323-335.

Malanotte-Rizzoli, P., Artale, V., Borzelli-Eusebi, G. L., Brenner, S., Crise, A., Gacic, M., ... & Triantafyllou, G. (2014). Physical forcing and physical/biochemical variability of the Mediterranean Sea: a review of unresolved issues and directions for future research. *Ocean Science*, *10*(3), 281-322.

Marotzke, J., & Scott, J. R. (1999). Convective mixing and the thermohaline circulation. *Journal of Physical Oceanography*, *29*(11), 2962-2970.

Mashayek, A., Ferrari, R., Merrifield, S., Ledwell, J. R., St Laurent, L., & Garabato, A. N. (2017). Topographic enhancement of vertical turbulent mixing in the Southern Ocean. *Nature communications*, 8(1), 1-12.

Meccia, V. L., Borghini, M., & Sparnocchia, S. (2015). Abyssal circulation and hydrographic conditions in the Western Ionian Sea during Spring–Summer 2007 and Autumn–Winter 2007–2008. *Deep Sea Research Part I: Oceanographic Research Papers*, *104*, 26-40.

Melet, A., Hallberg, R., Legg, S., & Nikurashin, M. (2014). Sensitivity of the ocean state to lee wave–driven mixing. *Journal of physical oceanography*, *44*(3), 900-921.

Miles, J. W. (1961). On the stability of heterogeneous shear flows. *Journal of Fluid Mechanics*, *10*(4), 496-508.

Millot, C., & Taupier-Letage, I. (2005). Circulation in the Mediterranean sea. *The Mediterranean Sea*, 29-66.

Munk, W. H. (1966). Abyssal recipes. In *Deep Sea Research and Oceanographic Abstracts* (Vol. 13, No. 4, pp. 707-730). Elsevier.

Munk, W. H. (1981). Internal waves and small-scale processes. *Evolution of physical oceanography*, 264-291.

Munk, W., & Wunsch, C. (1998). Abyssal recipes II: Energetics of tidal and wind mixing. *Deep Sea Research Part I: Oceanographic Research Papers*, 45(12), 1977-2010.

Musgrave, R., Pollmann, F., Kelly, S., & Nikurashin, M. (2022). The lifecycle of topographically-generated internal waves. In *Ocean mixing* (pp. 117-144). Elsevier.

Napolitano, E., Sannino, G., Artale, V., & Marullo, S. (2003). Modeling the baroclinic circulation in the area of the Sicily channel: The role of stratification and energy diagnostics. *Journal of Geophysical Research: Oceans*, 108(C7).

Nash, J. D., Kunze, E., Toole, J. M., & Schmitt, R. W. (2004). Internal tide reflection and turbulent mixing on the continental slope. *Journal of Physical Oceanography*, *34*(5), 1117-1134.

https://doi.org/10.5194/egusphere-2025-4762
Preprint. Discussion started: 9 October 2025

882 Nikurashin, M., & Ferrari, R. (2010a). Radiation and dissipation of internal waves generated by
883 geostrophic motions impinging on small-scale topography: Theory. *Journal of Physical*
884 *Oceanography*, *40*(5), 1055-1074.
885 Nikurashin, M., & Ferrari, R. (2010b). Radiation and dissipation of internal waves generated by
886 geostrophic motions impinging on small-scale topography: Application to the Southern
887 Ocean. *Journal of Physical Oceanography*, *40*(9), 2025-2042.

888 Nikurashin, M., & Ferrari, R. (2013). Overturning circulation driven by breaking internal waves in the
889 deep ocean. *Geophysical Research Letters*, *40*(12), 3133-3137.

890 Nikurashin, M., and Ferrari, R. (2011). Global energy conversion rate from geostrophic flows into
891 internal lee waves in the deep ocean. Geophysical Research Letters, 38, L08610.
892 https://doi.org/10.1029/2011GL046576

893 Oka, A., & Niwa, Y. (2013). Pacific deep circulation and ventilation controlled by tidal mixing away
894 from the sea bottom. *Nature communications*, *4*(1), 1-8.

895 Osborn, T. R., & Cox, C. S. (1972). Oceanic fine structure. *Geophysical Fluid Dynamics*, *3*(4), 321-
896 345.

897 Osborne, A. R., & Burch, T. L. (1980). Internal solitons in the Andaman Sea. *Science*, *208*(4443), 451-
898 460.

899 Pinardi, N., & Masetti, E. (2000). Variability of the large scale general circulation of the Mediterranean
900 Sea from observations and modelling: a review. *Palaeogeography, Palaeoclimatology,*
901 *Palaeoecology*, *158*(3-4), 153-173.

902 Pollmann, F. (2020). Global characterization of the ocean's internal wave spectrum. *Journal of*
903 *Physical Oceanography*, *50*(7), 1871-1891.
904 Pollmann, F., Eden, C., & Olbers, D. (2017). Evaluating the global internal wave model IDEMIX
905 using finestructure methods. *Journal of Physical Oceanography*, *47*(9), 2267-2289.

906 Polzin, K. L. (2010). Mesoscale eddy–internal wave coupling. Part II: Energetics and results from
907 PolyMode. *Journal of physical oceanography*, 40(4), 789-801.

908 Polzin, K. L., & Lvov, Y. V. (2011). Toward regional characterizations of the oceanic internal
909 wavefield. *Reviews of geophysics*, *49*(4).

910 Polzin, K. L., Garabato, A. C. N., Huussen, T. N., Sloyan, B. M., & Waterman, S. (2014). Finescale
911 parameterizations of turbulent dissipation. *Journal of Geophysical Research: Oceans*, 119(2), 1383-
912 1419.

913 Polzin, K. L., Naveira Garabato, A. C., Huussen, T. N., Sloyan, B. M., & Waterman, S. (2014).
914 Finescale parameterizations of turbulent dissipation. *Journal of Geophysical Research:*
915 *Oceans*, *119*(2), 1383-1419.

916 Polzin, K. L., Toole, J. M., Ledwell, J. R., & Schmitt, R. W. (1997). Spatial variability of turbulent
917 mixing in the abyssal ocean. *Science*, *276*(5309), 93-96.

918 Polzin, K., Kunze, E., Hummon, J., & Firing, E. (2002). The finescale response of lowered ADCP
919 velocity profiles. *Journal of Atmospheric and Oceanic Technology*, *19*(2), 205-224.

https://doi.org/10.5194/egusphere-2025-4762
Preprint. Discussion started: 9 October 2025

Roether, W., & Schlitzer, R. (1991). Eastern Mediterranean deep water renewal on the basis of chlorofluoromethane and tritium data. *Dynamics of Atmospheres and Oceans*, 15(3-5), 333-354.

Roether, W., Manca, B. B., Klein, B., Bregant, D., Georgopoulos, D., Beitzel, V., ... & Luchetta, A. (1996). Recent changes in eastern Mediterranean deep waters. *Science*, *271*(5247), 333-335.

Rubino, A., Falcini, F., Zanchettin, D., Bouche, V., Salusti, E., Bensi, M., ... & Capone, A. (2012). Abyssal undular vortices in the Eastern Mediterranean basin. *Nature communications*, *3*(1), 1-6.

Ruddick, B. (1983). A practical indicator of the stability of the water column to double-diffusive activity. *Deep Sea Research Part A. Oceanographic Research Papers*, *30*(10), 1105-1107.

Saenko, O. A., & Merryfield, W. J. (2005). On the effect of topographically enhanced mixing on the global ocean circulation. *Journal of Physical Oceanography*, *35*(5), 826-834.

Schlitzer, R., Roether, W., Oster, H., Junghans, H. G., Hausmann, M., Johannsen, H., & Michelato, A. (1991). Chlorofluoromethane and oxygen in the Eastern Mediterranean. *Deep Sea Research Part A. Oceanographic Research Papers*, 38(12), 1531-1551.

Schneider, A., Tanhua, T., Roether, W., & Steinfeldt, R. (2014). Changes in ventilation of the Mediterranean Sea during the past 25 year. *Ocean Science*, 10(1), 1-16.

Schroeder, K., Chiggiato, J., Bryden, H. L., Borghini, M., & Ben Ismail, S. (2016). Abrupt climate shift in the Western Mediterranean Sea. Scientific reports, 6(1), 23009.

Schroeder, K., Gasparini, G. P., Tangherlini, M., & Astraldi, M. (2006). Deep and intermediate water in the western Mediterranean under the influence of the Eastern Mediterranean Transient. *Geophysical Research Letters*, 33(21).

Seager, R., Osborn, T. J., Kushnir, Y., Simpson, I. R., Nakamura, J., & Liu, H. (2019). Climate variability and change of Mediterranean-type climates. *Journal of Climate*, 32(10), 2887-2915.

Send, U., & Testor, P. (2017). Direct observations reveal the deep circulation of the western Mediterranean Sea. *Journal of Geophysical Research: Oceans*, 122(12), 10091-10098.

Sheen, K. L., Brearley, J. A., Naveira Garabato, A. C., Smeed, D. A., Waterman, S., Ledwell, J. R., ... & Watson, A. J. (2013). Rates and mechanisms of turbulent dissipation and mixing in the Southern Ocean: Results from the Diapycnal and Isopycnal Mixing Experiment in the Southern Ocean (DIMES). *Journal of Geophysical Research: Oceans*, *118*(6), 2774-2792.

Simmons, H. L., Jayne, S. R., Laurent, L. C. S., & Weaver, A. J. (2004). Tidally driven mixing in a numerical model of the ocean general circulation. *Ocean Modelling*, *6*(3-4), 245-263.

Somot, S., Sevault, F., & Déqué, M. (2006). Transient climate change scenario simulation of the Mediterranean Sea for the twenty-first century using a high-resolution ocean circulation model. *Climate Dynamics*, 27(7), 851-879.

Sparnocchia, S., Gasparini, G. P., Astraldi, M., Borghini, M., & Pistek, P. (1999). Dynamics and mixing of the Eastern Mediterranean outflow in the Tyrrhenian basin. *Journal of Marine Systems*, *20*(1-4), 301-317.

https://doi.org/10.5194/egusphere-2025-4762
Preprint. Discussion started: 9 October 2025

Sparnocchia, S., Gasparini, G.P., Schroeder, K., Borghini, M. (2011). Oceanographic conditions in the NEMO region during the KM3NeT project (April2006–May2009). *Nucl. Instrum. Methods Phys. Res. A*, S87–S90. http://dx.doi.org/10.1016/j.nima.2010.06.231 626-627.

St. Laurent, L., Naveira Garabato, A. C., Ledwell, J. R., Thurnherr, A. M., Toole, J. M., & Watson, A. J. (2012). Turbulence and diapycnal mixing in Drake Passage. *Journal of Physical Oceanography*, 42(12), 2143-2152.

Stommel, H., & Arons, A. B. (1959). On the abyssal circulation of the world ocean—II. An idealized model of the circulation pattern and amplitude in oceanic basins. *Deep Sea Research (1953)*, *6*, 217-233.

Takahashi, A., Hibiya, T., & Naveira Garabato, A. C. (2021). Influence of the distortion of vertical wavenumber spectra on estimates of turbulent dissipation using the finescale parameterization: Eikonal calculations. *Journal of Physical Oceanography*, *51*(5), 1723-1733.

Theocharis, A., Klein, B., Nittis, K., & Roether, W. (2002). Evolution and status of the Eastern Mediterranean Transient (1997–1999). *Journal of Marine Systems*, 33, 91-116.

Thorpe, S. A. (2005). *The turbulent ocean*. Cambridge University Press.

Tsimplis, M. N., Zervakis, V., Josey, S. A., Peneva, E. L., Struglia, M. V., Stanev, E. V., ... & Oguz, T. (2006). Changes in the oceanography of the Mediterranean Sea and their link to climate variability. In *Developments in earth and environmental sciences* (Vol. 4, pp. 227-282). Elsevier.

Thurnherr 2012: The Finescale Response of Lowered ADCP Velocity Measurements Processed with Different Methods. https://journals.ametsoc.org/view/journals/atot/29/4/jtech-d-11-00158_1.xml. https://doi.org/10.1175/JTECH-D-11-00158.1

van Haren, H., & Gostiaux, L. (2011). Large internal waves advection in very weakly stratified deep Mediterranean waters. *Geophysical Research Letters*, 38(22).

Waldman, R., Brüggemann, N., Bosse, A., Spall, M., Somot, S., & Sevault, F. (2018). Overturning the Mediterranean thermohaline circulation. *Geophysical Research Letters*, 45(16), 8407-8415.

Walin, G. (1982). On the relation between sea-surface heat flow and thermal circulation in the ocean. *Tellus*, *34*(2), 187-195.

Waterhouse, A. F., et al. (2014). Global patterns of diapycnal mixing from measurements and models. Journal of Physical Oceanography, 44(7), 1854–1872. https://doi.org/10.1175/JPO-D-13-0133.1

Whalen, C. B., De Lavergne, C., Naveira Garabato, A. C., Klymak, J. M., MacKinnon, J. A., & Sheen, K. L. (2020). Internal wave-driven mixing: Governing processes and consequences for climate. *Nature Reviews Earth & Environment*, *1*(11), 606-621.

Wright, D. G., & Stocker, T. F. (1992). Sensitivities of a zonally averaged global ocean circulation model. *Journal of Geophysical Research: Oceans*, *97*(C8), 12707-12730.

Wunsch, C., & Ferrari, R. (2004). Vertical mixing, energy, and the general circulation of the oceans. *Annu. Rev. Fluid Mech.*, *36*, 281-314.

https://doi.org/10.5194/egusphere-2025-4762
Preprint. Discussion started: 9 October 2025

992 Wüst, G. (1961). On the vertical circulation of the Mediterranean Sea. *Journal of Geophysical*
993 *Research*, 66(10), 3261-3271.

994